The Astrophysical Journal Letters, 902:L2 (9pp), 2020 October 10 https://doi.org/10.3847/2041-8213/aba82a


# The X-Ray Reactivation of the Radio Bursting Magnetar SGR J1935+2154

A. Borghese[1,2], F. Coti Zelati[1,2], N. Rea[1,2], P. Esposito[3,4], G. L. Israel[5], S. Mereghetti[4], and A. Tiengo[3,4,6]
[1] Institute of Space Sciences (ICE, CSIC), Campus UAB, Carrer de Can Magrans s/n, E-08193, Barcelona, Spain; borghese@ice.csic.es
[2] Institut d'Estudis Espacials de Catalunya (IEEC), Carrer Gran Capità 2–4, E-08034 Barcelona, Spain
[3] Scuola Universitaria Superiore IUSS Pavia, Palazzo del Broletto, piazza della Vittoria 15, I-27100 Pavia, Italy
[4] INAF–Istituto di Astrofisica Spaziale e Fisica Cosmica di Milano, via A. Corti 12, I-20133 Milano, Italy
[5] INAF–Osservatorio Astronomico di Roma, via Frascati 33, I-00078 Monteporzio Catone, Italy
[6] Istituto Nazionale di Fisica Nucleare (INFN), Sezione di Pavia, via A. Bassi 6, I-27100 Pavia, Italy
*Received 2020 May 31; revised 2020 July 10; accepted 2020 July 20; published 2020 October 5*

## Abstract

A few years after its discovery as a magnetar, SGR J1935+2154 started a new burst-active phase on 2020 April 27, accompanied by a large enhancement of its X-ray persistent emission. Radio single bursts were detected during this activation, strengthening the connection between magnetars and fast radio bursts. We report on the X-ray monitoring of SGR J1935+2154 from ∼3 days prior to ∼3 weeks after its reactivation, using Swift, the Nuclear Spectroscopic Telescope Array (NuSTAR), and the Neutron Star Interior Composition Explorer (NICER). We detected X-ray pulsations in the NICER and NuSTAR observations, and constrained the spin period derivative to $|\dot{P}| < 3 \times 10^{-11}$ s s$^{-1}$ ($3\sigma$ c.l.). The pulse profile showed a variable shape switching between single and double-peaked as a function of time and energy. The pulsed fraction decreased from ∼34% to ∼11% (5–10 keV) over ∼10 days. The X-ray spectrum was well fit by an absorbed blackbody model with temperature decreasing from $kT_{\rm BB} \sim 1.6$ to 0.45–0.6 keV, plus a nonthermal power-law component ($\Gamma \sim 1.2$) observed up to ∼25 keV with NuSTAR. The 0.3–10 keV X-ray luminosity increased in less than 4 days from $\sim 6 \times 10^{33} d_{6.6}^2$ erg s$^{-1}$ to about $3 \times 10^{35} d_{6.6}^2$ erg s$^{-1}$ and then decreased again to $2.5 \times 10^{34} d_{6.6}^2$ erg s$^{-1}$ over the following 3 weeks of the outburst, where $d_{6.6}$ is the source distance in units of 6.6 kpc. We also detected several X-ray bursts, with properties typical of short magnetar bursts.

*Unified Astronomy Thesaurus concepts:* Neutron stars (1108); Magnetars (992); Radio pulsars (1353); X-ray bursts (1814); X-ray transient sources (1852)

## 1. Introduction

Magnetars are isolated X-ray pulsars with spin periods in the 0.3–12 s range and large spin-down rates, implying particularly strong surface dipolar magnetic fields of the order of $B \sim 10^{14}$–$10^{15}$ G (see Kaspi & Beloborodov 2017; Esposito et al. 2018 for recent reviews). These objects have a persistent X-ray luminosity of $L_X \sim 10^{31}$–$10^{36}$ erg s$^{-1}$, which is thought to be powered by the instabilities and decay of their extreme magnetic fields. Among isolated neutron stars, magnetars are the most variable, with an unpredictable bursting activity. They emit short (<1 s) and bright ($L_{\rm peak} \approx 10^{39}$–$10^{41}$ erg s$^{-1}$) bursts in the X-ray band, either sporadically or clustered in "forests" (e.g., Israel et al. 2008; Collazzi et al. 2015). These bursts are often accompanied by an enhancement of the X-ray persistent flux, up to three orders of magnitude above quiescence. Then, the flux usually relaxes back to the pre-outburst level on months/years timescales (Coti Zelati et al. 2018). Recently, magnetar traits have been observed also in high-*B* pulsars (e.g., Gavriil et al. 2008; Archibald et al. 2016), X-ray pulsars with dipolar fields as low as $6 \times 10^{12}$ G (e.g., Rea et al. 2010, 2012a), and the central source of the supernova remnant RCW 103 (e.g., D'Aì et al. 2016; Rea et al. 2016; Borghese et al. 2018). These findings have shown how magnetar-like emission might be more common within the neutron star population than previously expected.

SGR J1935+2154 (SGR J1935 hereafter) was discovered in 2014, when the Burst Alert Telescope (BAT) on board the Neil Gehrels Swift Observatory (Gehrels et al. 2004) triggered on a short burst (Stamatikos et al. 2014). A follow-up campaign confirmed the source as a magnetar with spin period $P \sim 3.25$ s and spin-down rate $\dot{P} \sim 1.43 \times 10^{-11}$ s s$^{-1}$, implying a dipole magnetic field $B \sim 4.4 \times 10^{14}$ G at the pole and characteristic age $\tau_c \sim 3.6$ kyr (Israel et al. 2016). SGR J1935 has been quite active since then, with intense outbursts in 2015 February and 2016 May and June (Younes et al. 2017b), and frequent bursting activity (Lin et al. 2020a).

SGR J1935 reactivated on 2020 April 27–28, emitting a forest of X-ray bursts (e.g., Palmer & BAT Team 2020; Younes et al. 2020) accompanied by an increase of the persistent X-ray flux, as is typical in magnetar outbursts. More interestingly, two millisecond radio bursts temporally coincident with a hard X-ray burst were detected from the direction of the source (Bochenek et al. 2020; Li et al. 2020; Mereghetti et al. 2020; Tavani et al. 2020; The CHIME/FRB Collaboration et al. 2020), strengthening the long suspected connection between magnetars and fast radio bursts (FRBs; see Cordes & Chatterjee 2019; Petroff et al. 2019 for reviews). However, besides these radio bursts, radio pulsed emission has not been detected so far from the source (e.g., Younes et al. 2017b; Lin et al. 2020b).

This Letter reports on the results of our monitoring campaign of SGR J1935 with Swift, the Nuclear Spectroscopic Telescope Array (NuSTAR), and the Neutron Star Interior Composition Explorer (NICER), covering the first ∼20 days since its reactivation. We describe the observations (Section 2) and report our timing and spectral analysis as well as a search for short bursts (Section 3). We discuss our findings in Section 4.

## 2. Observations and Data Reduction

We report the log of the observations used in this work in Table 1. Data reduction was performed using tools in the

**Table 1**
Observation Log and Blackbody Spectral Parameters

| Instrument[a] | Obs.ID | Start | Stop | Exposure (ks) | Count Rate[b] (counts $s^{-1}$) | $kT_{\rm BB}$ (keV) | $R_{\rm BB}$ (km) | Flux[c] ($10^{-11}$ cgs) |
|---|---|---|---|---|---|---|---|---|
| | | YYYY Mmm DD hh:mm:ss (TT) | | | | | | |
| Swift/XRT (PC) | 00033349044 | 2020 Apr 23 15:16:16 | 2020 Apr 23 15:49:27 | 2.0 | $0.012 \pm 0.002$ | … | … | 0.045[d] |
| Swift/XRT (PC) | 00968211001 | 2020 Apr 27 19:41:56 | 2020 Apr 27 20:15:09 | 1.8 | $0.37 \pm 0.01$ | $1.6^{+0.2}_{-0.1}$ | $0.49^{+0.12}_{-0.10}$ | $5.01^{+0.05}_{-0.59}$ |
| NICER/XTI | 3020560101 | 2020 Apr 28 00:38:31 | 2020 Apr 28 16:21:20 | 4.7 | $2.94 \pm 0.04$ | $0.80 \pm 0.02$ | $1.11 \pm 0.05$ | $2.49 \pm 0.12$ |
| Swift/XRT (PC) | 00033349045 | 2020 Apr 28 18:00:36 | 2020 Apr 28 21:37:41 | 2.9 | $0.077 \pm 0.005$ | $0.61^{+0.09}_{-0.10}$ | $0.99^{+0.39}_{-0.19}$ | $0.6 \pm 0.1$ |
| Swift/XRT (WT) | 00033349046 | 2020 Apr 29 13:07:57 | 2020 Apr 29 13:32:57 | 1.5 | $0.09 \pm 0.01$ | $0.36^{+0.15}_{-0.10}$ | $2.74^{+6.61}_{-1.08}$ | $0.69^{+0.09}_{-0.15}$ |
| NICER/XTI | 3020560102 | 2020 Apr 29 13:47:17 | 2020 Apr 29 14:05:20 | 1.1 | $0.96 \pm 0.05$ | $0.49 \pm 0.02$[e] | $1.47^{+0.17}_{-0.14}$ | $0.82^{+0.11}_{-0.08}$ |
| Swift/XRT (PC) | 00033349047 | 2020 Apr 29 17:54:22 | 2020 Apr 29 18:27:38 | 2.0 | $0.072 \pm 0.006$ | $0.44^{+0.07}_{-0.06}$ | $2.05^{+1.04}_{-0.49}$ | $0.52^{+0.08}_{-0.10}$ |
| NICER/XTI | 3655010101 | 2020 Apr 29 21:31:57 | 2020 Apr 29 21:48:40 | 0.8 | $0.78 \pm 0.04$ | $0.49 \pm 0.02$[e] | $1.88^{+0.15}_{-0.11}$ | $0.40 \pm 0.07$ |
| NICER/XTI | 3655010102 | 2020 Apr 30 00:37:56 | 2020 Apr 30 07:09:40 | 5.3 | $0.73 \pm 0.02$ | $0.49 \pm 0.02$[e] | $1.73^{+0.12}_{-0.09}$ | $0.40^{+0.05}_{-0.07}$ |
| NICER/XTI | 3020560103 | 2020 Apr 30 13:02:45 | 2020 Apr 30 13:17:20 | 0.8 | $0.72 \pm 0.04$ | $0.49 \pm 0.02$[e] | $1.83^{+0.16}_{-0.14}$ | $0.32^{+0.13}_{-0.07}$ |
| Swift/XRT (PC) | 00033349048 | 2020 Apr 30 05:29:05 | 2020 Apr 30 18:27:53 | 1.9 | $0.054 \pm 0.005$ | $0.44^{+0.11}_{-0.09}$ | $1.55^{+1.56}_{-0.48}$ | $0.46^{+0.02}_{-0.13}$ |
| Swift/XRT (WT) | 00033349049 | 2020 Apr 30 07:10:24 | 2020 Apr 30 11:47:56 | 1.5 | $0.05 \pm 0.01$ | $0.40^{+0.27}_{-0.40}$ | $1.84^{+8.70}_{-0.83}$ | $0.57 \pm 0.16$ |
| Swift/XRT (PC) | 00033349050 | 2020 May 1 02:03:14 | 2020 May 1 22:42:20 | 2.1 | $0.056 \pm 0.005$ | $0.63^{+0.09}_{-0.16}$ | $0.93^{+0.51}_{-0.19}$ | $0.36^{+0.19}_{-0.09}$ |
| Swift/XRT (WT) | 00033349051 | 2020 May 1 12:58:08 | 2020 May 1 13:20:56 | 1.4 | $0.05 \pm 0.01$ | $0.39^{+0.09}_{-0.08}$ | $2.98^{+2.74}_{-0.88}$ | $0.33^{+0.04}_{-0.15}$ |
| NuSTAR FPMA/B | 80602313002 | 2020 May 2 00:06:09 | 2020 May 2 20:31:09 | 37.1/36.9 | $0.175 \pm 0.003$ | $0.59^{+0.06}_{-0.05}$ | $0.85^{+0.35}_{-0.18}$ | $0.32 \pm 0.01$ |
| Swift/XRT (WT) | 00033349053 | 2020 May 2 11:50:05 | 2020 May 2 13:28:56 | 0.7 | $0.06 \pm 0.02$ | $0.69^{+0.14}_{-0.18}$ | $0.97^{+0.52}_{-0.26}$ | $0.30^{+0.52}_{-0.09}$ |
| Swift/XRT (PC) | 00033349052 | 2020 May 2 16:33:41 | 2020 May 2 23:02:54 | 1.2 | $0.027 \pm 0.005$ | $0.71^{+0.14}_{-0.27}$ | $0.69^{+0.32}_{-0.22}$ | $0.18^{+0.63}_{-0.01}$ |
| Swift/XRT (WT) | 00033349055 | 2020 May 3 12:55:54 | 2020 May 3 13:23:56 | 1.7 | $0.020 \pm 0.009$ | $0.45^{+0.23}_{-0.15}$ | $1.24^{+3.10}_{-0.50}$ | $0.27^{+0.06}_{-0.15}$ |
| Swift/XRT (PC) | 00033349054 | 2020 May 3 22:23:05 | 2020 May 3 22:48:52 | 1.5 | $0.050 \pm 0.006$ | $0.68^{+0.02}_{-0.18}$ | $0.93^{+0.41}_{-0.18}$ | $0.24^{+0.4}_{-0.01}$ |
| Swift/XRT (PC) | 00033349056 | 2020 May 4 01:47:23 | 2020 May 4 18:04:51 | 3.4 | $0.040 \pm 0.003$ | $0.48^{+0.08}_{-0.07}$ | $1.29^{+0.65}_{-0.29}$ | $0.28^{+0.03}_{-0.06}$ |
| Swift/XRT (WT) | 00033349057 | 2020 May 4 12:40:56 | 2020 May 4 13:07:56 | 1.6 | $0.07 \pm 0.01$ | $0.66^{+0.18}_{-0.20}$ | $0.85^{+0.97}_{-0.24}$ | $0.53^{+0.05}_{-0.20}$ |
| Swift/XRT (PC) | 00033349058 | 2020 May 5 03:17:19 | 2020 May 5 13:01:52 | 1.9 | $0.034 \pm 0.004$ | $0.53^{+0.09}_{-0.17}$ | $1.15^{+1.82}_{-0.27}$ | $0.15^{+0.15}_{-0.09}$ |
| Swift/XRT (WT) | 00033349059 | 2020 May 5 20:40:09 | 2020 May 5 21:02:56 | 1.4 | $0.05 \pm 0.01$ | $0.55^{+0.08}_{-0.07}$ | $1.37^{+0.54}_{-0.31}$ | $0.19^{+0.07}_{-0.04}$ |
| Swift/XRT (PC) | 00033349060 | 2020 May 6 06:36:44 | 2020 May 6 08:20:52 | 1.3 | $0.031 \pm 0.005$ | $0.46^{+0.10}_{-0.08}$ | $1.50^{+1.06}_{-0.42}$ | $0.18^{+0.04}_{-0.07}$ |
| Swift/XRT (PC) | 00033349061 | 2020 May 7 09:30:09 | 2020 May 7 20:56:54 | 3.7 | $0.035 \pm 0.003$ | $0.47 \pm 0.09$ | $1.57^{+0.99}_{-0.33}$ | $0.23^{+0.08}_{-0.13}$ |
| Swift/XRT (PC) | 00033349062 | 2020 May 10 04:28:08 | 2020 May 10 22:15:52 | 3.2 | $0.043 \pm 0.004$ | $0.63^{+0.02}_{-0.13}$ | $0.99^{+0.32}_{-0.16}$ | $0.23 \pm 0.11$ |
| Swift/XRT (WT) | 00033349063 | 2020 May 10 06:01:43 | 2020 May 10 10:56:56 | 3.2 | $0.030 \pm 0.007$ | $0.51 \pm 0.10$ | $1.51^{+1.06}_{-0.37}$ | $0.24^{+0.05}_{-0.08}$ |
| NuSTAR FPMA/B | 80602313004 | 2020 May 10 23:51:09 | 2020 May 11 20:31:09 | 38.5/38.2 | $0.140 \pm 0.002$ | $0.52 \pm 0.04$ | $1.03^{+0.32}_{-0.20}$ | $0.27 \pm 0.01$ |
| NICER/XTI | 3020560104 | 2020 May 11 14:30:54 | 2020 May 11 16:18:40 | 1.3 | $0.54 \pm 0.04$ | $0.49 \pm 0.02$[e] | $1.70^{+0.14}_{-0.11}$ | $0.16 \pm 0.01$ |
| Swift/XRT (WT) | 00033349064 | 2020 May 13 02:22:52 | 2020 May 13 07:29:55 | 1.9 | $0.56^{+0.14}_{-0.17}$[f] | $0.69 \pm 0.10$ | $0.95^{+1.29}_{-0.26}$ | $0.17^{+0.03}_{-0.06}$ |
| Swift/XRT (WT) | 00033349065 | 2020 May 13 09:03:52 | 2020 May 13 10:30:56 | 1.3 | $0.56^{+0.14}_{-0.17}$[f] | $0.69 \pm 0.10$ | $0.95^{+1.29}_{-0.26}$ | $0.17^{+0.03}_{-0.06}$ |
| Swift/XRT (WT) | 00033349066 | 2020 May 15 00:31:07 | 2020 May 15 03:58:39 | 3.5 | $0.059 \pm 0.006$ | $0.46 \pm 0.07$ | $1.70^{+0.86}_{-0.39}$ | $0.24^{+0.04}_{-0.10}$ |

**Notes.**
[a] The instrumental setup is indicated in brackets: PC = photon counting, WT = windowed timing.
[b] Count rate, computed after removing bursts, in the 0.3–10 keV range for Swift, in the 1–5 keV band for NICER, and in the 3–25 keV range for NuSTAR summing up the two FPMs.
[c] Observed 0.3–10 keV flux in units of $10^{-11}$ erg $cm^{-2}$ $s^{-1}$.
[d] The flux is estimated using WEBPIMMS (see the text for details).
[e] The blackbody temperature was tied up among these data sets (see the text for details).
[f] These observations were combined to increase the signal-to-noise ratio.

HEASOFT package (version 6.27.2). Photon arrival times were referred to the solar system barycenter using the source Chandra position (R.A. = $19^{\rm h}34^{\rm m}55\overset{\rm s}{.}598$, decl. = $+21°53'47\overset{''}{.}79$, J2000.0; Israel et al. 2016) and the JPL planetary ephemeris DE 200. In the following, we adopt a distance of 6.6 kpc (Zhou et al. 2020; see also Mereghetti et al. 2020) and quote all uncertainties at $1\sigma$ confidence level (c.l.).

### 2.1. *Swift*

After the Swift/BAT trigger, SGR J1935 was monitored almost daily with the Swift/X-ray Telescope (XRT; Burrows et al. 2005) either in photon counting (PC; timing resolution of 2.51 s) or windowed timing (WT; 1.8 ms) modes. The data were reprocessed and analyzed with standard prescriptions.

In the first XRT observation performed after the BAT trigger, a dust scattering ring was detected around the source, extending from $\sim 1'$ to $2'$ (Kennea et al. 2020; Mereghetti et al. 2020). This structure was no longer observed in a pointing performed the following day (a detailed study of this structure will be presented in a future paper). We collected the source photons from a 20 pixel circle (1 pixel = $2\overset{''}{.}36$). Background counts were extracted from a region of the same size for WT data and an annulus with radii of 100 and 150 pixels, centered on the source, for the PC observations.

### 2.2. *NuSTAR*

SGR J1935 was observed with NuSTAR (Harrison et al. 2013) twice, on 2020 May 2 and 11. The two focal plane modules FPMA and FPMB observed the source for a total on-source exposure time of 75.6 and 75.1 ks, respectively. We used the tool NUPIPELINE to create cleaned event files and filter out passages through the South Atlantic Anomaly. The source counts were collected within a circular region of radius 100″, while the background was estimated from a 100″ circle on the same chip of the target. In both pointings, SGR J1935 is detected until $\sim$25 keV. We ran the script NUPRODUCTS to extract light curves and spectra, and generate response files for both FPMs.

### 2.3. *NICER*

NICER (Gendreau et al. 2012) observed SGR J1935 six times for a total on-source exposure time of $\sim$14 ks. The data were processed via the NICERDAS pipeline, with the tool NICERL2 with standard filtering criteria. The background count rate and spectra were computed from NICER observations of the RXTE blank-field regions using NIBACKGEN3C50.

## 3. Analysis and Results

### 3.1. *Timing Analysis*

For the timing analysis, we selected events in the 1–5 keV energy band for NICER and 3–20 keV for NuSTAR. The data sets of NICER observations IDs 3655010101, 3655010102, and 3020560103 performed on 2020 April 29–30 were merged to increase the source signal-to-noise ratio. We did not include Swift/XRT observations in our timing analysis due to their poor counting statistics.

We calculated a power density spectrum (PDS) for all time series to search for the spin signal, assuming a $3.5\sigma$ detection threshold for the signal (using the algorithm by Israel & Stella 1996), taking into account all the frequencies in the PDS. Pulsations were significantly detected over a blind search only during the first NuSTAR observation. The signal was then found in the second NuSTAR observation and in the NICER combined pointings IDs 3655010101 + 3655010102 + 3020560103 by looking in the range of periods $P \pm \Delta P$ (at $3\sigma$; the $\dot{P}$ component can be neglected) around the value measured in the first NuSTAR data set. The period values were then refined by means of a phase-fitting technique. We obtained the following results: $P = 3.24731(1)$ s for the combined NICER data sets (2020 April 29–30), $P = 3.247331(3)$ s for the first NuSTAR observation (2020 May 2), and $P = 3.24734(1)$ s for the second NuSTAR observation (2020 May 11). The above uncertainties and the variable pulse profile (see below) did not allow us to phase-connect coherently the NICER and NuSTAR observations. These period measurements imply an upper limit on the spin period derivative of $|\dot{P}| < 3 \times 10^{-11}$ s s$^{-1}$ ($3\sigma$ c.l.), a factor of about 2 above the value inferred during the 2014 outburst (Israel et al. 2016).

Figure 1 shows the pulse profiles at different epochs and as a function of energy. The profile shape varies considerably in time, changing from quasi-sinusoidal on 2020 April 29–30 to double-peaked on 2020 May 2 and 11 (the separation between the two peaks is about half a rotational cycle). The profile shape is also highly variable with energy in the NuSTAR data sets, the second peak (at phase $\sim$0.6–0.7) being more prominent above 5 keV and dominating above 10 keV in the first observation.

The background-subtracted pulsed fraction (defined as the semiamplitude of the sinusoidal functions describing the pulse divided by the source average count rate) decreased by a factor of $\approx$3 between 2020 May 2 and 11 (in the 3–5 and 5–10 keV ranges; see Figure 1). No pulsations were detected over the 10–20 keV band in the second NuSTAR observation, and we set a $3\sigma$ upper limit on the pulsed fraction of $\sim$15%.

### 3.2. *Spectral Analysis*

The spectral analysis was performed with the XSPEC fitting package. We adopted the TBABS model (Wilms et al. 2000) to describe the photoelectric absorption by the interstellar medium. The NuSTAR and NICER background-subtracted spectra were grouped in at least 50 and 20 counts per bin, respectively. The Swift/XRT spectra were grouped according to a minimum number of counts variable from observation to observation. We used the Cash statistic to compute model parameters and their uncertainties.

Figure 1 shows the spectra extracted from nearly simultaneous NuSTAR and Swift/XRT data. The broadband spectrum is well described by an absorbed blackbody model plus a power-law component accounting for the emission above 10 keV. The hydrogen column density was held fixed to $N_{\rm H} = 2.3 \times 10^{22}$ cm$^{-2}$ in the fits, i.e., the value derived by Coti Zelati et al. (2018; this is compatible with that given by Younes et al. 2017b). For the first epoch (2020 May 2), the best-fitting values are $kT_{\rm BB} = 0.59^{+0.06}_{-0.05}$ keV, $R_{\rm BB} = 0.85^{+0.35}_{-0.18}$ km, and photon index $\Gamma = 1.17 \pm 0.06$ ($C$-stat = 160.24 for 146 degrees of freedom, dof). For the second epoch (2020 May 11), we derived $kT_{\rm BB} = 0.52 \pm 0.04$ keV, $R_{\rm BB} = 1.03^{+0.32}_{-0.20}$ km, and $\Gamma = 1.22 \pm 0.06$ ($C$-stat= 112.17/145 dof). The observed fluxes were $(6.9 \pm 0.1) \times 10^{-12}$ and $5.9^{+0.3}_{-0.1} \times 10^{-12}$ erg cm$^{-2}$ s$^{-1}$ (0.3–25 keV), chronologically, giving luminosities of $(4.01 \pm 0.08) \times 10^{34} d_{6.6}^2$ and $(3.46 \pm 0.08) \times 10^{34} d_{6.6}^2$ erg s$^{-1}$, where $d_{6.6}$ is the source distance in units of 6.6 kpc. At both epochs, the power-law component accounted

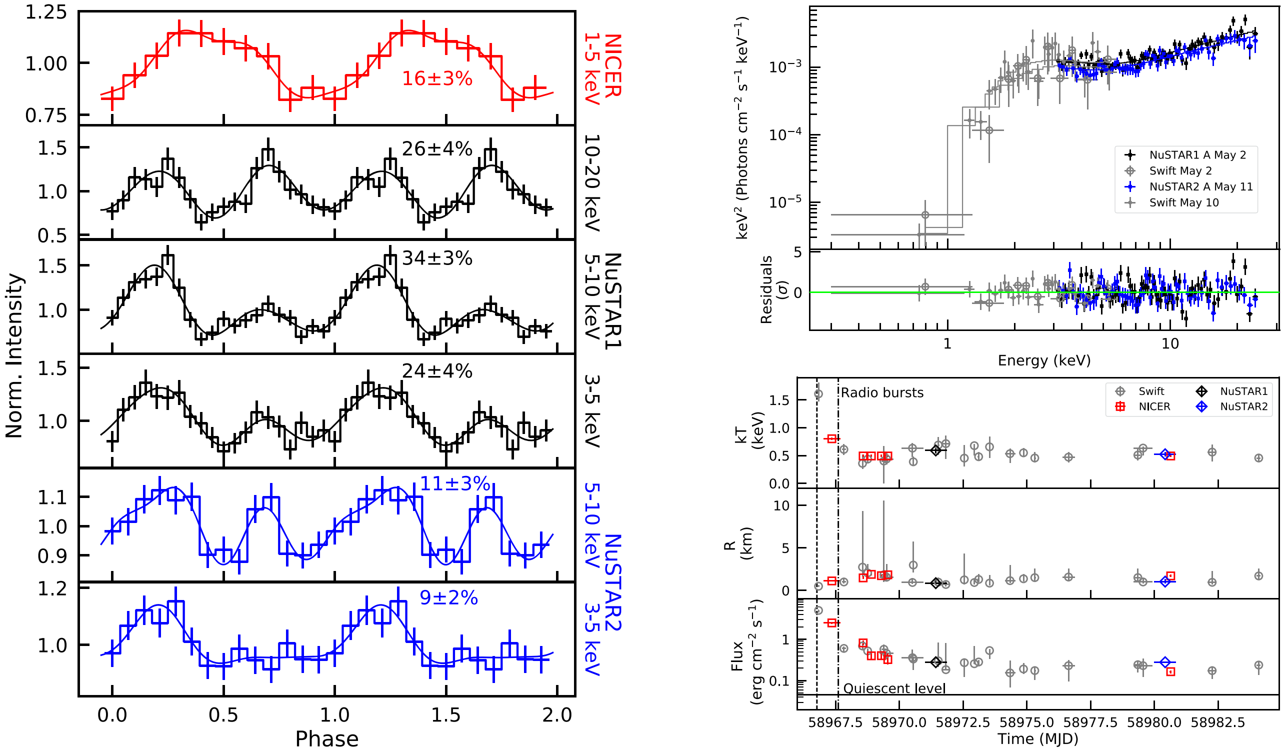


**Figure 1.** Left: energy-resolved background-subtracted pulse profiles of SGR J1935 extracted from NICER and NuSTAR data. The profiles at the different epochs have been aligned so as to have the pulse minimum at phase 0. The best-fitting models obtained by using two (for NICER) and three (NuSTAR) sinusoidal components (fundamental plus harmonics) are shown with solid lines. The corresponding pulsed fractions are reported in each panel. Top right: broadband unfolded spectra extracted from the quasi-simultaneous Swift/XRT and NuSTAR data on 2020 May 2 and 11. The best-fitting model is plotted with a solid line. We show only the FPMA spectra for display purposes. The bottom panel shows the post-fit residuals in units of standard deviations. Bottom right: temporal evolution of the blackbody temperature (top), radius (middle), and observed flux in units of $10^{-11}$ erg cm$^{-2}$ s$^{-1}$ (0.3–10 keV; bottom). The dashed line denotes the epoch of the first BAT trigger (MJD 58966.7683; Palmer & BAT Team 2020). The dashed–dotted line marks the epoch of the two bright radio bursts (MJD 58967.6072; Bochenek et al. 2020; The CHIME/FRB Collaboration et al. 2020). The solid line in the bottom panel marks the quiescent flux, $\sim 4.5 \times 10^{-13}$ erg cm$^{-2}$ s$^{-1}$.

for ∼86% of the total observed flux and its luminosity varied from $(3.23 \pm 0.09) \times 10^{34} d_{6.6}^2$ to $(2.84 \pm 0.07) \times 10^{34} d_{6.6}^2$ erg s$^{-1}$ (0.3–25 keV).

We then fit the same model to the Swift/XRT spectra jointly, and repeated the same procedure for the NICER spectra ($N_{\rm H}$ was fixed to the above value). To avoid covariance between the values of the blackbody temperature and normalization due to the limited energy band adopted for NICER spectra (1–5 keV), we tied up the temperature across all data sets except for the first one. First, we allowed the photon index to vary in the fits. However, we could not obtain meaningful constraints on this parameter over the energy range covered by Swift and NICER. We then repeated the analysis by fixing it to $\Gamma = 1.2$, i.e., the value measured using the NuSTAR observations. We obtained $C$-stat = 134.95 for 111 dof for the Swift data and $C$-stat = 447.71 for 480 dof for the NICER data.

The blackbody temperature reached a value of $kT_{\rm BB} = 1.61^{+0.20}_{-0.14}$ keV about 75 minutes after the first BAT trigger on 2020 April 27 at 18:26:20 UT (Palmer & BAT Team 2020). It decreased to $(0.80 \pm 0.02)$ keV in the following day, and attained values in the range 0.45–0.6 keV over the last ∼10 days of our monitoring (Table 1; Figure 1). During the first ∼20 days of this new active phase, the observed flux dropped from $5.01^{+0.05}_{-0.59} \times 10^{-11}$ to $2.3^{+0.4}_{-1.0} \times 10^{-12}$ erg cm$^{-2}$ s$^{-1}$ (0.3–10 keV; Table 1; Figure 1). These values translate into a luminosity of $(3.2 \pm 0.3) \times 10^{35} d_{6.6}^2$ and $(2.5 \pm 0.2) \times 10^{34} d_{6.6}^2$ erg s$^{-1}$ (0.3–10 keV), respectively. An XRT observation performed on 2020 April 23 (only 4 days prior to the outburst onset) found SGR J1935 in quiescence with a net count rate of $0.012 \pm 0.002$ counts s$^{-1}$ (0.3–10 keV), corresponding to an observed flux of $\sim 4.5 \times 10^{-13}$ erg cm$^{-2}$ s$^{-1}$ and a luminosity of $\sim 5.8 \times 10^{33} d_{6.6}^2$ erg s$^{-1}$ (assuming an absorbed blackbody spectrum with $kT_{\rm BB} = 0.5$ keV, $N_{\rm H} = 2.3 \times 10^{22}$ cm$^{-2}$).

### 3.3. Burst Search and Properties

We inspected the light curves of all observations for the presence of short bursts. Our search algorithm estimates the Poisson probability for an event to be a random fluctuation compared to the average number of counts per bin in the full observation, considering the total number of time bins $N$. We applied this algorithm to light curves binned with different time resolutions ($2^{-4}$, $2^{-5}$, and $2^{-6}$ s) to be sensitive to bursts of different durations, except for the Swift/XRT PC-mode event files that were binned at the available timing resolution (2.5073 s). Bins having a probability smaller than $10^{-4}(N N_{\rm trials})^{-1}$ are identified as bursts ($N_{\rm trials}$ is the number of different time resolutions adopted for the search). In Table 2, we report the epochs of the bursts referred to the solar system barycenter. Fluence and duration are given for the bursts detected in the NICER and NuSTAR data sets. Their light curves are shown in Figure 2. We do not report on the ∼25 short bursts detected in the first NICER observation (Obs. ID 3020560101; see Table 1 of Younes et al. 2020) due to the complex light curve and instrument saturation problems.

**Table 2**
Log of X-ray Bursts Detected in All Data Sets Except for the First NICER Observation (ID 3020560101; See the Text for Details)

| Instrument | Obs.ID[a] | Burst Epoch YYYY Mmm DD hh:mm:ss (TDB) | Fluence[b] (counts) | Duration[c] (ms) |
|---|---|---|---|---|
| Swift/XRT (PC)[d] | 00968211001 #1 | 2020 Apr 27 19:46:52 | … | … |
| | #2 | 19:57:22 | … | … |
| | #3 | 20:03:38 | … | … |
| | #4 | 20:09:12 | … | … |
| | #5 | 20:14:42 | … | … |
| | #6 | 20:15:30 | … | … |
| Swift/XRT (WT)[d] | 00033349046 #1 | 13:12:34 | … | … |
| | #2 | 13:19:38 | … | … |
| | #3 | 13:21:59 | … | … |
| | #4 | 13:33:48 | … | … |
| NICER/XTI | 3655010101 #1 | 2020 Apr 29 21:49:09 | 8 | 62.5 |
| NICER/XTI | 3655010102 #1 | 2020 Apr 30 00:51:27 | 6 | 31.25 |
| | #2 | 05:21:38.89 | 7 | 62.5 |
| | #3 | 06:56:59 | 11 | 62.5 |
| Swift/XRT (WT)[d] | 00033349049 #1 | 2020 Apr 30 08:53:44 | … | … |
| Swift/XRT (WT)[d] | 00033349051 #1 | 2020 May 1 13:03:55 | … | … |
| NuSTAR | 80602313002 #1 | 2020 May 2 05:43:12 | 11 | 31.25 |
| | #2 | 10:19:46 | 13 | 31.25 |
| | #3 | 10:27:46 | 46 | 0.125 |
| Swift/XRT (WT)[d] | 00033349059 #1 | 2020 May 5 20:50:38 | … | … |
| Swift/XRT (WT)[d] | 00033349063 #1 | 2020 May 10 07:50:37 | … | … |
| NuSTAR | 80602313004 #1 | 2020 May 11 00:33:00 | 43 | 93.75 |
| | #2 | 00:47:14 | 7 | 62.5 |
| | #3 | 09:46:00 | 7 | 62.5 |
| | #4 | 13:20:16 | 25 | 46.875 |
| | #5 | 18:22:15 | 7 | 62.5 |
| | #6 | 19:38:10 | 7 | 62.5 |
| NICER/XTI | 3020560104 #1 | 2020 May 11 14:47:00 | 8 | 62.5 |
| Swift/XRT (WT)[d] | 00033349064 #1 | 2020 May 13 02:27:45 | … | … |
| | #2 | 07:10:44 | … | … |
| | #3 | 07:12:16 | … | … |
| | #4 | 07:16:22 | … | … |
| | #5 | 07:27:04 | … | … |
| Swift/XRT (WT)[d] | 00033349065 #1 | 2020 May 13 09:12:39 | … | |
| | #2 | 10:24:18 | … | |
| Swift/XRT (WT)[d] | 00033349066 #1 | 2020 May 15 01:06:18 | … | |
| | #2 | 02:16:50 | … | … |
| | #3 | 02:25:54 | … | … |
| | #4 | 02:36:56 | … | … |
| | #5 | 02:43:10 | … | … |
| | #6 | 02:43:19 | … | … |
| | #7 | 03:53:54 | … | … |
| | #8 | 03:55:00 | … | … |

**Notes.**
[a] The notation $\#N$ corresponds to the burst number in a given observation.
[b] The fluence refers to the 0.3–10 keV range for NICER/XTI and 3–79 keV for NuSTAR.
[c] The duration has to be considered as an approximate value. We estimated it by summing the 15.625 ms time bins showing enhanced emission for the structured bursts, and by setting it equal to the coarser time resolution at which the burst is detected in all the other cases.
[d] Fluence and maximum durations are not reported for the bursts detected by Swift/XRT owing to uncertainties related to the detector saturation limits.

We extracted the spectra only for those events with at least 30 net counts, that is, two bursts detected in the NuSTAR observations (80602313002 #3 and 80602313004 #1 in Table 2). We fitted the spectra using single-component models (a power law, a blackbody, and an optically thin thermal bremsstrahlung). The blackbody and power-law model fits gave a satisfactory description for both events with a goodness probability[7] of ∼55% and ∼40%, respectively. For the blackbody model, we derived a temperature equivalent to $(2.9 \pm 0.5)$ keV for 80602313002 #3 and $(3.9 \pm 0.7)$ keV for 80602313004 #1. The corresponding fluxes were $(1.0 \pm 0.3) \times 10^{-8}$ and $(1.8 \pm 0.6) \times 10^{-8}$ erg cm$^{-2}$ s$^{-1}$ in the 3–79 keV energy range, converting to luminosities of $(5.3 \pm 1.5) \times 10^{37} d_{6.6}^2$ and $(9.3 \pm 3.1) \times 10^{37} d_{6.6}^2$ erg s$^{-1}$.

## 4. Discussion

Since its discovery in 2014, the magnetar SGR J1935 has been a prolific source, showing numerous X-ray outbursts and frequent bursting activity. We presented here the results of an

[7] https://heasarc.gsfc.nasa.gov/xanadu/xspec/manual/node84.html

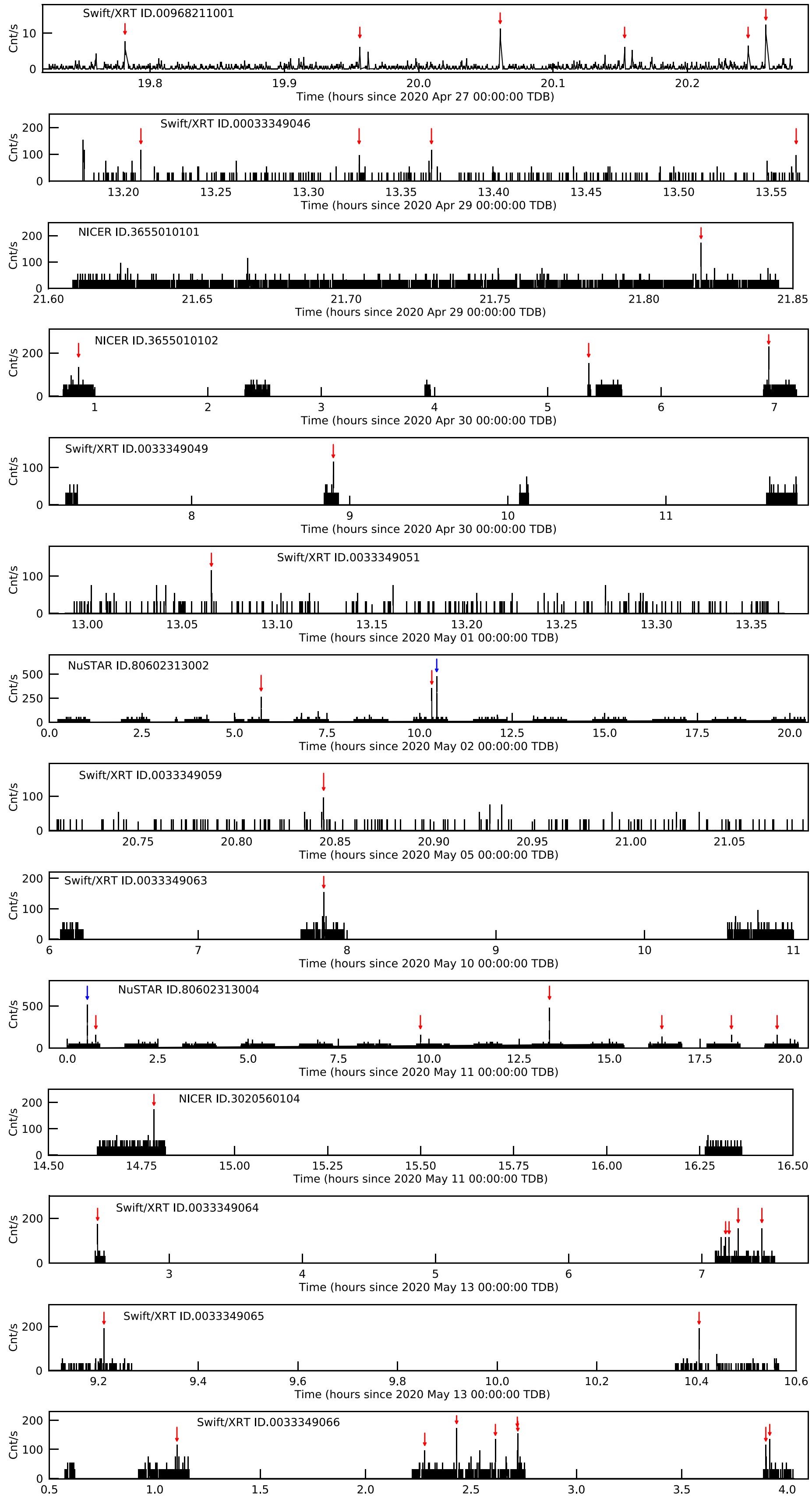


**Figure 2.** Light curves of SGR J1935 extracted from the Swift/XRT (0.3–10 keV), NuSTAR (3–79 keV), and NICER (0.3–10 keV) data in which we detected bursts. All bursts are marked by arrows (in blue for the two cases for which we performed a spectral analysis). The light curves were binned at 62.5 ms in all cases except for the data of the first Swift/XRT PC-mode observation (ID 00968211001), binned at 2.5073 s.

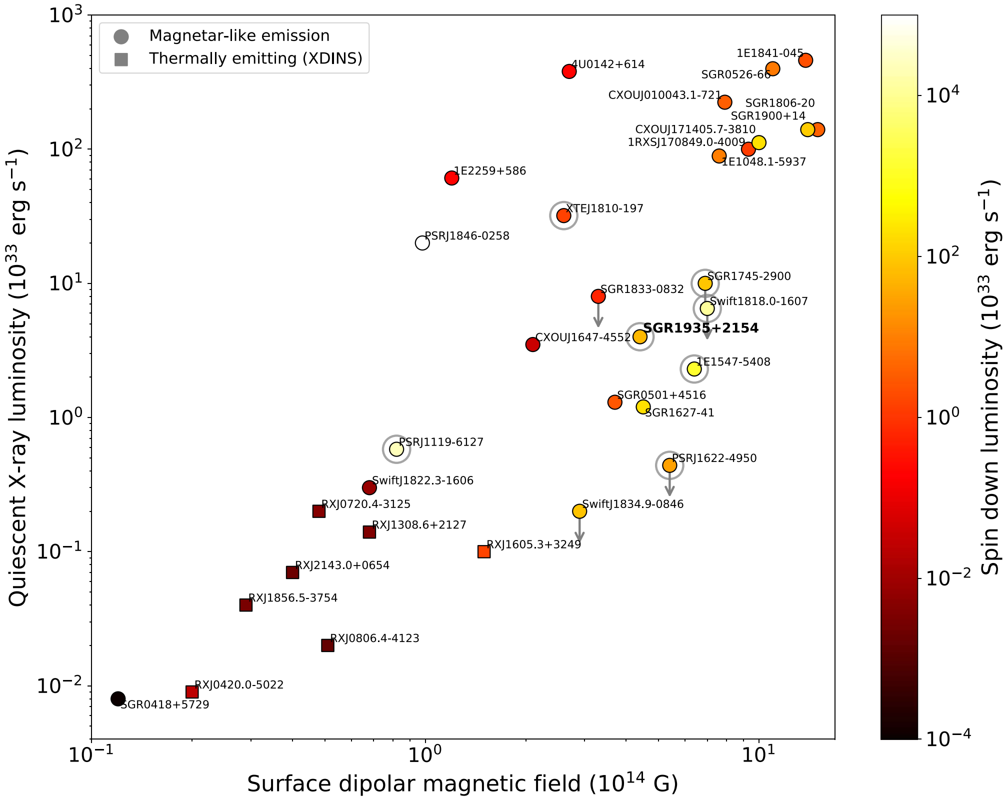


**Figure 3.** Quiescent X-ray luminosity of magnetars as a function of their dipolar magnetic field at the pole. Circles denote radio-loud magnetars, either in the form of bursts (SGR J1935; in bold) or pulsed emission (other sources). Markers are color-coded according to the spin-down power of each source. Values are from the Magnetar Outburst Online Catalogue (http://magnetars.ice.csic.es/; Coti Zelati et al. 2018), with updates for PSR J1622−4950 (Camilo et al. 2018), SGR 1806−20 (Younes et al. 2017a), and Swift J1818.0−1607 (Esposito et al. 2020).

intensive X-ray monitoring campaign of this source over about 3 weeks since the end of 2020 April, when it emitted a forest of X-ray bursts, and two bright radio millisecond bursts with characteristics strongly reminiscent of FRBs (Bochenek et al. 2020; The CHIME/FRB Collaboration et al. 2020).

1. *Spin period and pulse profiles*. We detected the source spin period in the combined NICER data sets acquired on 2020 April 29–30, and in both NuSTAR data sets on 2020 May 2 and 11. Unfortunately, the spacing between the few detections, and the uncertainties on the periods, prevented us from extracting a phase-connected timing solution. The spin period measurements at the different epochs allowed us to set an upper limit on the period derivative of $|\dot{P}| < 3 \times 10^{-11}$ s s$^{-1}$ (at $3\sigma$ c.l.). This limit is compatible with the spin-down rate of $\dot{P} \sim 1.43 \times 10^{-11}$ s s$^{-1}$ derived by Israel et al. (2016) in 2014, using a phase-connected timing analysis.

The double-peaked morphology of the NuSTAR pulse profiles is markedly different from the quasi-sinusoidal modulation observed in the NICER observation a few days before and in previous X-ray observations of the source (Israel et al. 2016). Timing noise and large pulse profile changes (in time and energy) are common during magnetar outbursts (e.g., Dib & Kaspi 2014; Esposito et al. 2018 for a review, and references therein), especially following X-ray bursting activity. The magnetar magnetosphere is subject to rapid changes before setting to a new quiescent configuration, which are responsible for the fast profile variations especially in the hard X-rays, where the emission is dominated by nonthermal photons. These changes might also lead to the formation of new bundles and hot spots on the surface, modifying the pulse profile also in the soft X-ray range.

2. *Luminosity, spectral evolution, and bursting activity*. About three days before its reactivation, SGR J1935 was observed by Swift/XRT at a luminosity of $\sim 5.8 \times 10^{33} d_{6.6}^2$ erg s$^{-1}$ (0.3–10 keV). Following the source reactivation, the X-ray luminosity reached a peak value of $\sim 3.2 \times 10^{35} d_{6.6}^2$ erg s$^{-1}$, making this event the most powerful outburst detected from SGR J1935 so far. The luminosity then dropped by more than one order of magnitude, down to $\sim 2.5 \times 10^{34} d_{6.6}^2$ erg s$^{-1}$ about 3 weeks later. However, this is still a factor $\sim 4$ larger than the pre-outburst level. A similar rapid decay pattern was also observed for the strong outbursts in 2016 May and June (Younes et al. 2017b) and, overall, is not uncommon for magnetars in outburst (Coti Zelati et al. 2018).

During the entire monitoring, SGR J1935 showed a thermal spectrum in the soft X-rays well described by an absorbed blackbody model quickly cooling from a temperature of $\sim 1.6$ to $\sim 0.45$–0.6 keV. Emission was detected up to $\sim 25$ keV in the NuSTAR observations. The spectral shape was identical at the two epochs, and was adequately modeled by a power-law model with index $\Gamma \sim 1.2$ and luminosity $\sim 4 \times 10^{34} d_{6.6}^2$ erg s$^{-1}$ (extrapolated to the 10–50 keV energy range). Hard X-ray emission from SGR J1935 was seen also in a NuSTAR pointing performed $\sim 5$ days after the 2015 outburst onset. In that case, the high-energy spectrum could be described by a slightly harder power-law component ($\Gamma \sim 0.9$) with a lower luminosity, $\sim 1 \times 10^{34} d_{6.6}^2$ erg s$^{-1}$ (10–50 keV; Younes et al. 2017b). However, the spectral evolution during this last outburst is different from that observed in the previous events, where the luminosity decay could be ascribed to the evolution of the high-energy component (Younes et al. 2017b).

The bursting activity of SGR J1935 during this new outburst is not dissimilar from that previously observed in this and other magnetars. However, such activity is not so prolific in all magnetars, and it is expected to depend on the age of the source and the tangled configuration of its magnetic field (Perna & Pons 2011; Viganò et al. 2013). A very rough proxy for it is provided by the quiescent X-ray luminosity, which is predicted to be higher in magnetars with a more tangled and powerful magnetic field in the crust, since they are subject to larger crustal currents and *B*-field crustal dissipation (see Figure 3). A significant anticorrelation between magnetar quiescent luminosities and their luminosity increases in outburst was observed (Pons & Rea 2012; Coti Zelati et al. 2018), suggesting the existence of a limiting luminosity of $\sim 10^{36}$ erg s$^{-1}$ for magnetar outbursts (regardless of the source quiescent level), which also holds for the case of SGR J1935.

3. *Comparison with other magnetars and FRBs*. Comparing the short X-ray bursts and outburst emitted by SGR J1935 with those of the other Galactic magnetars, they are perfectly in line with expectations. There is nothing in the X-ray emission properties of this magnetar that would make it peculiar in any aspect (Coti Zelati et al. 2018). However, the simultaneous detection of radio bursts with a bright magnetar-like burst (Bochenek et al. 2020; Mereghetti et al. 2020; The CHIME/FRB Collaboration et al. 2020) showed for the first time that magnetar bursts might have bright radio counterparts. This result is particularly interesting in the context of the physical interpretation of FRBs, bright millisecond-duration transients from distant galaxies. Their brightness temperatures imply a coherent radio emission, suggesting a connection with pulsar emission mechanisms. Several repeating FRBs have been discovered (Spitler et al. 2014, 2016), reinforcing their proposed interpretation in terms of young bursting magnetars in other galaxies (e.g., Popov & Postnov 2013; Margalit et al. 2020, and references therein).

Radio pulsed emission was so far restricted to five magnetars (see Figure 3). Such emission is at variance with the typical radio pulsar emission, and it is always connected to some extent with the magnetar X-ray activation. However, similarly to radio pulsars, all radio-loud magnetars have a large spin-down power compared to their radio-quiet siblings, and quiescent X-ray luminosity below their rotational power (with the exception of XTE J1810−197; Rea et al. 2012b; Coti Zelati et al. 2018 and Figure 3). SGR J1935 has a high rotational power, but so far it did not show any radio pulsations (Younes et al. 2017b; Lin et al. 2020b), while surprisingly emitting radio bursts during the outburst we report here. From the study of the bursting activity of this source, it becomes clear that (1) not all X-ray magnetar bursts necessarily have a radio counterpart (see also Archibald et al. 2020), and (2) many radio bursts from magnetars might have been missed due to the lack of large field-of-view instruments in the radio band. Hence, it might be a common characteristic after all. Future detections will shed light on these millisecond radio bursts, their connection (or not) with faint radio pulsations (i.e., bright single pulses), and their preferred X-ray burst counterparts. Population synthesis studies will allow a comparison between their rates and luminosity distributions and those observed in FRBs.

This research is based on observations with NICER (NASA), NuSTAR (CalTech/NASA/JPL), and Swift (NASA/ASI/UK). We thank the NICER, NuSTAR, and Swift teams for promptly scheduling our observations. We made use of public Swift and NICER observations asked by the CHIME/FRB collaboration and the NICER team, that we acknowledge. We thank Roberto Turolla and Andrea Possenti for useful suggestions. We acknowledge support from the PHAROS COST Action (CA16214). A.B. and F.C.Z. are supported by Juan de la Cierva fellowships. A.B., F.C.Z., and N.R. are supported by grants SGR2017-1383, PGC2018-095512-BI00, and the ERC Consolidator grant "MAGNESIA" (No. 817661). G.L.I., S.M., and A.T. acknowledge financial support from the Italian MIUR through PRIN grant 2017LJ39LM. G.L.I. also acknowledges funding from ASI-INAF agreements I/037/12/0 and 2017-14-H.O.

*Facilities:* NICER, NuSTAR, Swift (XRT).

*Software:* HEASoft (v6.27.2), FTOOLS (v6.27; Blackburn et al. 1995), XSPEC (v12.11.0h; Arnaud 1996), NICERDAS (v7a), NuSTARDAS (v1.9.2), MATPLOTLIB (v3.2.1; Hunter 2007), NUMPY (v1.18.4; van der Walt et al. 2011).

## ORCID iDs

A. Borghese https://orcid.org/0000-0001-8785-5922
F. Coti Zelati https://orcid.org/0000-0001-7611-1581
N. Rea https://orcid.org/0000-0003-2177-6388
P. Esposito https://orcid.org/0000-0003-4849-5092
G. L. Israel https://orcid.org/0000-0001-5480-6438
S. Mereghetti https://orcid.org/0000-0003-3259-7801
A. Tiengo https://orcid.org/0000-0002-6038-1090

## References

Archibald, R. F., Kaspi, V. M., Tendulkar, S. P., & Scholz, P. 2016, ApJL, 829, L21
Archibald, R. F., Scholz, P., Kaspi, V. M., Tendulkar, S. P., & Beardmore, A. P. 2020, ApJ, 889, 160
Arnaud, K. A. 1996, in ASP Conf Ser. 101, Astronomical Data Analysis Software and Systems V, ed. G. H. Jacoby & J. Barnes (San Francisco, CA: ASP), 17
Blackburn, J. K. 1995, in ASP Conf. Ser. 77, Astronomical Data Analysis Software and Systems IV, ed. R. A. Shaw, H. E. Payne, & J. J. E. Hayes (San Francisco, CA: ASP), 367
Bochenek, C. D., Ravi, V., Belov, K. V., et al. 2020, arXiv:2005.10828
Borghese, A., Coti Zelati, F., Esposito, P., et al. 2018, MNRAS, 478, 741
Burrows, D. N., Hill, J. E., Nousek, J. A., et al. 2005, SSRv, 120, 165
Camilo, F., Scholz, P., Serylak, M., et al. 2018, ApJ, 856, 180
Collazzi, A. C., Kouveliotou, C., van der Horst, A. J., et al. 2015, ApJS, 218, 11
Cordes, J. M., & Chatterjee, S. 2019, ARA&A, 57, 417
Coti Zelati, F., Rea, N., Pons, J. A., Campana, S., & Esposito, P. 2018, MNRAS, 474, 961
D'Aì, A., Evans, P. A., Burrows, D. N., et al. 2016, MNRAS, 463, 2394
Dib, R., & Kaspi, V. M. 2014, ApJ, 784, 37
Esposito, P., Rea, N., Borghese, A., et al. 2020, ApJL, 896, L30
Esposito, P., Rea, N., & Israel, G. L. 2018, in Timing Neutron Stars: Pulsations, Oscillations and Explosions, ed. T. Belloni, M. Mendez, & C. Zhang (Berlin: Springer) in press (arXiv:1803.05716)
Gavriil, F. P., Gonzalez, M. E., Gotthelf, E. V., et al. 2008, Sci, 319, 1802
Gehrels, N., Chincarini, G., Giommi, P., et al. 2004, ApJ, 611, 1005
Gendreau, K. C., Arzoumanian, Z., & Okajima, T. 2012, Proc. SPIE, 8443, 844313
Harrison, F. A., Craig, W. W., Christensen, F. E., et al. 2013, ApJ, 770, 103
Hunter, J. D. 2007, CSE, 9, 90
Israel, G. L., Esposito, P., Rea, N., et al. 2016, MNRAS, 457, 3448
Israel, G. L., Romano, P., Mangano, V., et al. 2008, ApJ, 685, 1114
Israel, G. L., & Stella, L. 1996, ApJ, 468, 369
Kaspi, V. M., & Beloborodov, A. M. 2017, ARA&A, 55, 261

Kennea, J. A., Beardmore, A. P., Page, K. L., & Palmer, D. M. 2020, ATel, 13679, 1

Li, C. K., Lin, L., Xiong, S. L., et al. 2020, arXiv:2005.11071

Lin, L., Göğüş, E., Roberts, O. J., et al. 2020a, ApJ, 893, 156

Lin, L., Zhang, C. F., Wang, P., et al. 2020b, arXiv:2005.11479

Margalit, B., Beniamini, P., Sridhar, N., & Metzger, B. D. 2020, arXiv:2005.05283

Mereghetti, S., Savchenko, V., Ferrigno, C., et al. 2020, ApJL, 898, L29

Palmer, D. M. & BAT Team 2020, GCN, 27665, 1, https://gcn.gsfc.nasa.gov/gcn3/27665.gcn3

Perna, R., & Pons, J. A. 2011, ApJL, 727, L51

Petroff, E., Hessels, J. W. T., & Lorimer, D. R. 2019, A&ARv, 27, 4

Pons, J. A., & Rea, N. 2012, ApJL, 750, L6

Popov, S. B., & Postnov, K. A. 2013, arXiv:1307.4924

Rea, N., Borghese, A., Esposito, P., et al. 2016, ApJL, 828, L13

Rea, N., Esposito, P., Turolla, R., et al. 2010, Sci, 330, 944

Rea, N., Israel, G. L., Esposito, P., et al. 2012a, ApJ, 754, 27

Rea, N., Pons, J. A., Torres, D. F., & Turolla, R. 2012b, ApJL, 748, L12

Spitler, L. G., Cordes, J. M., Hessels, J. W. T., et al. 2014, ApJ, 790, 101

Spitler, L. G., Scholz, P., Hessels, J. W. T., et al. 2016, Natur, 531, 202

Stamatikos, M., Malesani, D., Page, K. L., & Sakamoto, T. 2014, GCN, 16520, 1

Tavani, M., Casentini, C., Ursi, A., et al. 2020, arXiv:2005.12164

The CHIME/FRB Collaboration, Sankau, K., Andersen, B. C., et al. 2020, arXiv:2005.10324

van der Walt, S., Colbert, S. C., & Varoquaux, G. 2011, CSE, 13, 22

Viganò, D., Rea, N., Pons, J. A., et al. 2013, MNRAS, 434, 123

Wilms, J., Allen, A., & McCray, R. 2000, ApJ, 542, 914

Younes, G., Baring, M. G., Kouveliotou, C., et al. 2017a, ApJ, 851, 17

Younes, G., Baring, M. G., Kouveliotou, C., et al. 2020, arXiv:2006.11358

Younes, G., Kouveliotou, C., Jaodand, A., et al. 2017b, ApJ, 847, 85

Zhou, P., Zhou, X., Chen, Y., et al. 2020, arXiv:2005.03517